arXiv:2203.15070v2 [cond-mat.mtrl-sci] 28 Jun 2022

Is There a Polaron Signature in Angle-Resolved Photoemission of $CsPbBr_3$?

Maryam Sajedi,[1,2] Maxim Krivenkov,[1] Dmitry Marchenko,[1] Jaime Sánchez-Barriga,[1] Anoop K. Chandran,[3,4] Andrei Varykhalov,[1] Emile D. L. Rienks,[1] Irene Aguilera[5],* Stefan Blügel[3], and Oliver Rader[1]

[1] *Helmholtz-Zentrum Berlin für Materialien und Energie, Albert-Einstein-Str. 15, 12489 Berlin, Germany*

[2] *Institut für Physik und Astronomie, Universität Potsdam, Karl-Liebknecht-Str. 24/25, 14476 Potsdam, Germany*

[3] *Peter Grünberg Institut and Institute for Advanced Simulation, Forschungszentrum Jülich and JARA, 52425 Jülich, Germany*

[4] *Department of Physics, RWTH Aachen University, 52056 Aachen, Germany and*

[5] *Institute of Energy and Climate Research, IEK-5 Photovoltaics, Forschungszentrum Jülich, 52425 Jülich, Germany*

The formation of large polarons has been proposed as reason for the high defect tolerance, low mobility, low charge carrier trapping, and low nonradiative recombination rates of lead halide perovskites. Recently, direct evidence for large-polaron formation has been reported from a 50 % effective mass enhancement in angle-resolved photoemission of $CsPbBr_3$ over theory for the orthorhombic structure. We present in-depth band dispersion measurements of $CsPbBr_3$ and GW calculations which lead to almost identical effective masses at the valence band maximum of $0.203 \pm 0.016\ m_0$ in experiment and $0.226\ m_0$ in orthorhombic theory. We argue that the effective mass can be explained solely on the basis of electron-electron correlation and large-polaron formation cannot be concluded from photoemission data.

Lead halide perovskites have in recent years become a most important material class for solar cells approaching a tandem-cell efficiency of 30 % [1] as well as light-emitting diodes, semiconductor lasers, and radiation detectors [2]. They behave very differently from other semiconductors in that they are highly tolerant toward defects [3, 4] while showing long carrier lifetimes in the microsecond range and large carrier diffusion length [5]. The reason for these advantageous properties is, however, not well understood, which makes it difficult to optimize the charge carrier dynamics of this material class further [6–8]. The following possibly relevant factors have been reviewed: the influence of trap states on recombination [7, 9], polarons [6–8], combinations of the two [7], ferroelectric domains and boundaries [8], Rashba effect [8], and photon recycling [7].

Carrier mobilities turn out to be characteristically low. For single-crystal $CsPbBr_3$, a mobility of 143 $cm^2/(Vs)$ has been measured at room temperature [10] which, for comparison, is 5 times smaller than for the inorganic semiconductor GaN employed in light-emitting diodes [11]. To explain this property, electron-phonon interaction has been analyzed with the result that initially considered acoustic phonon scattering [12] is negligible in methylammonium lead iodide ($MAPbI_3$) and $CsPbI_3$ and the dominant contributions are from longitudinal optical (LO) phonons, which display very similar modes in the two materials [13]. Since these are ionic solids, it has been suggested that large polaron should form at intermediate electron-phonon coupling strength and could explain the combination of four properties [14]: the long carrier diffusion length and long lifetimes at modest mobilities, electron-hole recombination rates as low as in single-crystal inorganic semiconductors, a temperature dependence of the mobility $\mu \propto T^{-3/2}$, and exceptionally low carrier scattering rate also for hot carriers [15]. The concept of a large-polaron refers to its extent over several lattice sites and is associated with a coherent bandlike transport, the mobility of which decreases with increasing temperature. The effect on the mobility is intensively being discussed with a recently predicted reduction by a factor of 2 at low temperature and an enhancement at high temperature [16]. The idea to connect polaron formation with recombination rates is based on a short-range repulsion of oppositely charged large polarons [17].

When electron-phonon coupling is stronger, small polarons should form. These are associated with hopping-type transport and would lead to increasing mobility with increasing temperature. While the formation of small polarons has been predicted by density functional theory calculations [18], $\mu(T)$ data have been interpreted in favor of large-polaron formation [6, 19]. An early estimate of the effective mass of charge carriers from the measured mobility and the mean free path from the momentum relaxation time arrived at room-temperature values in the range of 10-300 electron masses m_0 [14].

The conditions for polaron formation have been investigated in several experiments. Zhu *et al.* [20, 21] conducted time-resolved photoluminescence experiments and found hot fluorescence emission with 100 ps lifetimes in $MAPbBr_3$ but not in $CsPbBr_3$. It was concluded that the organic cation is crucial and dynamic screening protects energetic carriers via large-polaron formation. Time-resolved two-photon photoemission and Kerr-effect measurements indicate that large polarons form due to the deformation of the $PbBr_3^-$ framework, irrespective of

the cation type [21, 22].

Frost *et al.* [23] theoretically investigated the thermalization kinetics for above-band-gap photoexcitation. The authors modeled effective masses of (transient) excitons and polarons in $MAPbI_3$. They calculated for $MAPbI_3$ the polaron coupling constants and estimated the polaron size based on the Fröhlich model as 26.8 Å (electron) and 25.3 Å (hole) at room temperature. They concluded that the one order of magnitude higher thermal conductivity of $CsPbI_3$ as compared to $MAPbI_3$ leads to faster cooling of polarons [23]. *Ab initio* calculations of transport including multiphonon coupling have recently shown good agreement with transport experiments where also the difference between thick single crystals and thin polycrystalline films of $MAPbI_3$ has been resolved through consideration of photon recycling [24]. Using *ab initio* many-body GW calculations with and without this multiphonon coupling, Ref. [25] predicts that polarons in the hybrid perovskite $MAPbI_3$ cause a mass enhancement of 28 %. Such effective mass renormalization could be tested by angle-resolved photoelectron spectroscopy (ARPES).

ARPES is a powerful tool to investigate the electronic band dispersion of charge carriers and the interaction with excitations such as phonons [26]. For example, in the polar compound anatase TiO_2 where transport is polaronic [27], photoemission spectral weight is transferred from the bulk quasiparticle band to photoemission satellites [28]. These satellites were described by phonon energies $\hbar\omega_0 = 108$ meV in agreement with a measured LO phonon mode. Second, the effective mass was determined as 0.7 m_0, as compared to the band mass 0.42 m_0 from density-functional theory (DFT), meaning a mass renormalization of 70 % [28]. Thirdly, the polaron contributions to the electron spectral function, including quasiparticle properties and satellites, have been calculated by a cumulant approach [29]. By comparison to calculations without electron-phonon coupling, a theoretical mass enhancement of 73 % was obtained [29], in good agreement with the ARPES experiment [28] and a large-polaron radius of 57 Å.

Also for the surface electronic structure of $SrTiO_3$, which is a polaronic conductor as well [30], a distinct satellite feature is seen in ARPES and two satellites can be fitted with phonon energies of 90 [31] to 100 meV [32].

Recently, Puppin *et al.* [33] investigated polaron formation in $CsPbBr_3$ by ARPES. The valence band maximum (VBM) at the R point was determined by tracing binding energy and effective mass with photon energy, i. e., with the electron wave vector perpendicular to the surface, $\mathbf{k}_\perp$. Comparison with DFT for orthorhombic $CsPbBr_3$ of 0.17 m_0 (0.12 m_0 for cubic) showed that the measured effective hole mass of $m_h^* = 0.26$ m_0 is enhanced by 50 % which was interpreted as direct experimental evidence that charge carriers form large polarons [33].

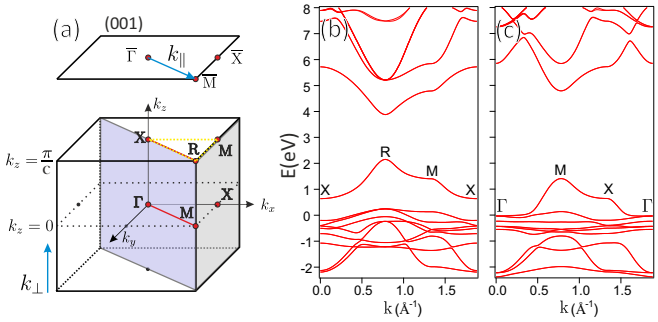


FIG. 1. (a) Cubic bulk and surface Brillouin zones, bulk paths $\Gamma - \mathrm{M}$ and $X - R$ projected onto $\overline{\Gamma} - \overline{\mathrm{M}}$ in the surface Brillouin zone. Yellow dashed line shows the $\mathrm{X} - \mathrm{R} - \mathrm{M} - \mathrm{X}$ path. (b),(c) Calculated GW band dispersions of $CsPbBr_3$ for the cubic phase presented for $\mathbf{k}_z = \pi/\mathrm{c}$ and $\mathbf{k}_z = 0$ planes, respectively. See Fig. S4 in the Supplemental Material for the orthorhombic bands.

For the present Letter, we have investigated $CsPbBr_3$ by ARPES experiments and by GW calculations. We obtain experimental and theoretical results very different from the previous work and we discuss possible reasons. In fact, experimental and theoretical effective masses are very similar and do not indicate large-polaron formation.

$CsPbBr_3$ single crystals have been grown by the antisolvent vapor-assisted crystallization method, adapted from Ref. [34]. ARPES has been performed with a hemispherical Scienta R8000 analyzer at the ARPES-1[2] and RGBL-2 instruments at BESSY-II using linearly polarized undulator radiation. Experiments have been done with freshly cleaved surfaces at room temperature as described previously (see Ref. [35] and its Supplemental Material for details on sample growth and the ARPES experiment). The base pressure of the instruments was better than 2×10^{-10} mbar and the spatial resolution in ARPES ~ 100 μm. For our calculations, we used the one-shot GW method (G_0W_0) as implemented in the all-electron FLEUR [36] and SPEX [37] codes, fully taking into account the spin-orbit coupling [38] (see Supplemental Material [39], which contains Refs. [40–45]).

Figure 1 shows the calculated GW bands for the cubic structure. Structural details such as lattice parameter of 6.017 Å are taken from [46]. Although $CsPbBr_3$ is orthorhombic at room temperature (tetragonal above 361 K and cubic above 403 K [47–49]), ARPES measurements at room temperature follow the band dispersion for the cubic phase [33]. The VBM is situated at the R point which is formed by antibonding orbitals, typical of the lead halide perovskites [50, 51]. $CsPbBr_3$ has a large experimental band gap of around 2.37 eV at room temperature [52]. Band gaps are not appropriately described by DFT in the local-density or generalized-gradient approximations. Even with the more advanced HSE06 hybrid functional, a band gap of only about 1.17 eV is obtained for $CsPbBr_3$ [53]. We use, therefore, many-body

perturbation theory in the GW approximation to calculate quasiparticle self-energy corrections for the electronic states, which yields results that are directly comparable with ARPES measurements. These do not include electron-phonon coupling and are therefore well suited as bare bands in the search for polaronic mass enhancement. The band gap we obtain for the cubic structure is 1.74 eV (Fig. 1). Note that GW calculations in two previous works [33, 54] lead to smaller band gaps of 1.05 and 0.94 eV, respectively. We tackle the question for this difference in our benchmarking calculations in the Supplemental Material [39], which contains Refs. [46, 55–59].

Figures 2(a) and 2(b) show overview ARPES spectra of $CsPbBr_3$ (100). Pb 6s states with little dispersion, as well as Br 4p states forming the VBM are marked by arrows. Figure 2(c) displays normal-emission measurements (i. e., at $\overline{\Gamma}$) as a function of photon energy between $h\nu = 21$ and 83 eV, with 2 eV steps.

These data show a symmetric behavior about the wave vector $\mathbf{k}_\perp = 3.66$ Å^{-1}. Since the VBM is not expected to occur in normal emission ($\overline{\Gamma}$), we can only determine critical points Γ and from extrema in the band dispersion. We distinguish X from Γ through the dispersion of the Pb 6s-Br 4p states [51] at around 9 eV binding energy, which are running downward from Γ to X. Our assignment of $\mathbf{k}_\perp = 3.66$ Å^{-1} to the X point in the simple model of free-electron final states corresponds to an inner potential of $V_0 = 9.6$ eV.

The location of the R point (projected on $\overline{\mathrm{M}}$) is directly revealed by a $\mathbf{k}_\parallel$-dependent plot at 1.5 eV binding energy, which is near the energy of the VBM [Fig. 2(f)].

We also show a second binding energy of 2.2 eV [Fig. 2(e)] to confirm that the contours around the VBM close in at 29 and 54 eV photon energies, which are therefore assigned as the R point [see the second derivative plot of Fig. 2(e) in the Supplemental Material [39]].

This corresponds to a slightly different inner potential of 5.3 eV. In order to verify the reproducibility of VBM selection, we have repeated the photon-energy-dependent experiments for the range of 14-43 eV with 1 eV steps. We demonstrate the $\mathbf{k}_\perp$ dispersions around the first R point ($h\nu = 29$ eV) at two binding energies (2.59 and 1.67 eV) in Figs. 2(g) and 2(h).

In Fig. 3 we show the band dispersion along $\overline{\Gamma} - \overline{\mathrm{M}}$ for various photon energies. At first, the binding energy of the local maximum (which is related to the plots in Fig. 2) is evaluated and confirms $h\nu = 29$ eV as the VBM. Moreover, it is seen that the dispersion at 29 eV appears narrower than those at the other photon energies. This is confirmed by the fits of dispersions and effective masses [Fig. 3(a)–3(h)]. We have repeated the measurement at 29 eV for three more samples (see Fig. S1, Supplemental Material [39]) and obtained m_h^* values of altogether 0.19, 0.23, 0.20, and 0.19 m_0, giving an average of 0.203±0.016 m_0 (standard deviation). It should be noted that the previous value of 0.26 m_0 at $h\nu = 33.5$ eV [33] connects

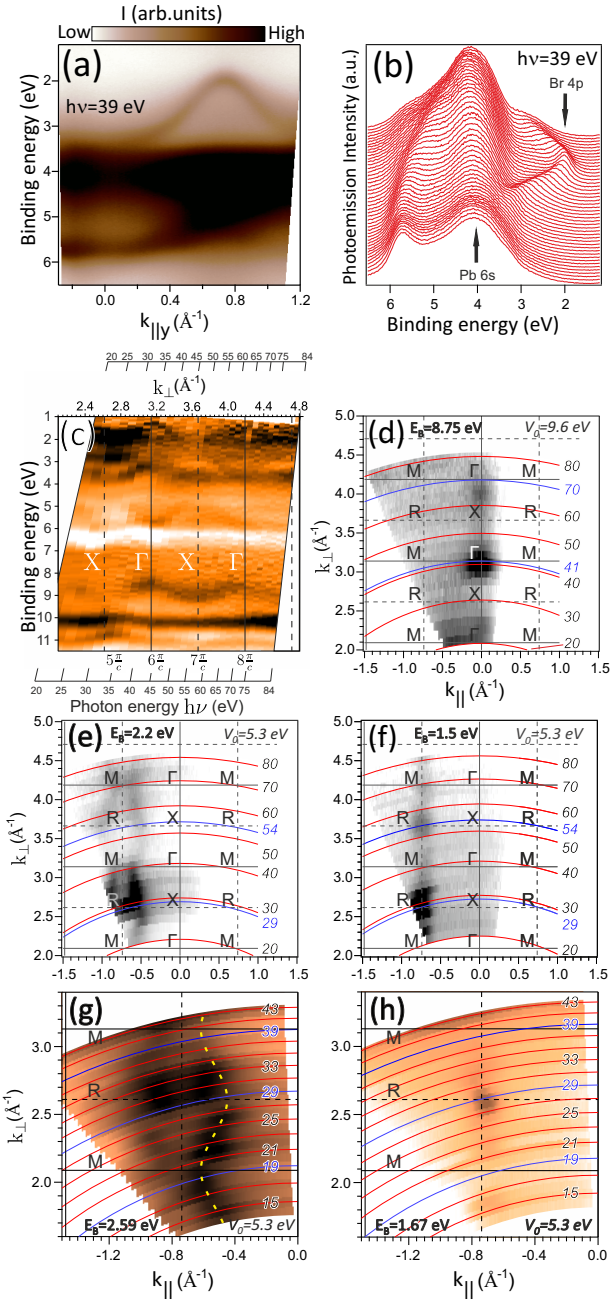


FIG. 2. ARPES determination of the photon energy that corresponds to the valence band maximum. (a,b) ARPES at $h\nu = 39$ eV. (c) Photon energy-dependent measurements taken at normal emission (dI/dE), converted to momentum space corresponding to the $\Gamma - X - \Gamma$ bulk direction. (d)–(h) ARPES intensity plots in momentum ($k_\perp$, $k_\parallel$) space extracted from photon-energy-dependent measurements (in eV) along $\overline{\Gamma} - \overline{\mathrm{M}}$ for (d) $V_0 = 9.6$ eV, indicating dispersions around Γ point, and (e),(f) $V_0 = 5.3$ eV near R point for two different binding energies (E_B). (g),(h) Intensity plots in ($k_\perp$, $k_\parallel$) extracted from another $h\nu$-dependent experiment for a different sample for two binding energies around the first R point. (a)–(f) Measured with horizontal and (g),(h) circular light polarization.

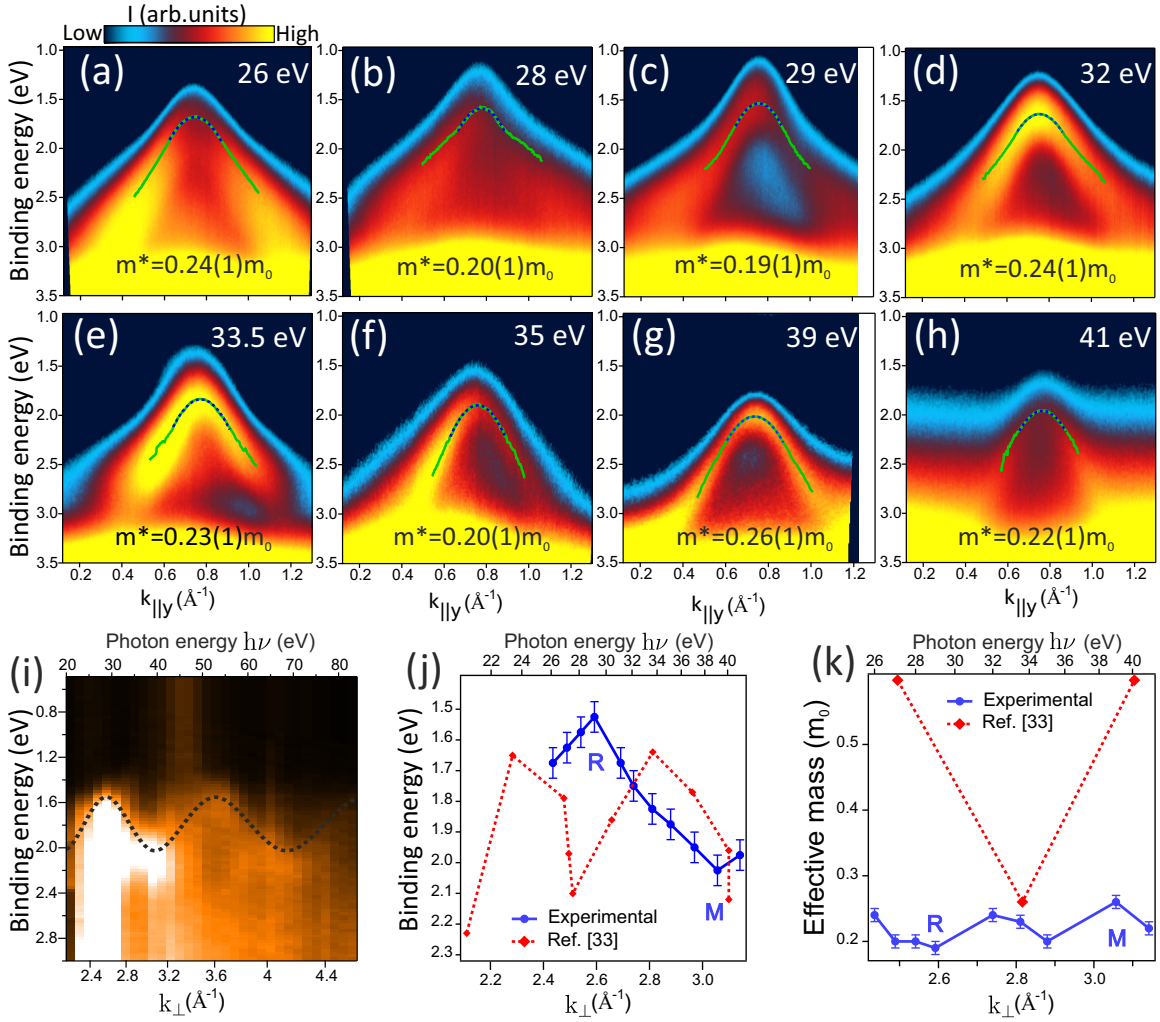


FIG. 3. (a)–(h) ARPES data along the $\overline{\Gamma}-\overline{\mathrm{M}}-\overline{\Gamma}$ direction for various photon energies. Numbers at the right indicate the corresponding photon energies. (i) Photon-energy dependence taken at $\overline{\mathrm{M}}$ point (dashed line guides the eye). (j) Energy of local maxima and (k) effective mass m_{h}^{*} vs. photon energy and $\mathbf{k}_{\perp}$ compared to Ref. [33]. $\mathbf{k}_{\perp}$ axis is converted from photon energies using $V_0 = 5.3$ eV. The binding energy of the topmost band in (j) has been determined from the individual spectra to have better precision than taking it from the overall $\mathbf{k}_{\perp}$ dependence (i).

to our measurement [0.23 m_0 see Fig. 3(k)], but the assignment to R does not. Our different values for V_0 for final states at $\overline{\Gamma}$ and $\overline{\mathrm{M}}$ shift the expected R point by only $\sim$ 2.5 eV in photon energy and do not explain the different assignment. It appears that the previous assignment of $m_{\mathrm{h}}^{*} = 0.26\ m_0$ is rather a consequence of higher m_{h}^{*} values $> 0.5\ m_0$ at 27 eV and 40 eV (Fig. S5 of Ref. [33]), which we cannot confirm (we obtain 0.24 m_0 at 26 eV, 0.26 m_0 at 39 eV, 0.22 m_0 at 41 eV). The identification of high-symmetry points corresponds also well with the overall $\mathrm{k}_{\perp}$ dispersion taken at $\overline{\mathrm{M}}$, see Figs. 3(i) and 3(j).

We compare the measured effective mass with our GW calculations. From our calculations, we obtain $m_{\mathrm{h}}^{*} = 0.15\ m_0$ (gap 1.74 eV) for the cubic structure at R evaluated along $X-R$, which is smaller than our ARPES value. It has been shown that the orthorhombic structure leads to a larger effective mass than the cubic one [33]. By DFT using the HSE functional, 0.12 m_0 was obtained for cubic and 0.17 m_0 for the orthorhombic structure used to derive the mass enhancement of 50 % [33]. Even though the band gap was underestimated by the calculation (1.17 eV), its effect on the effective mass was found to be less than 10 % [33]. A similar behavior was reported by Becker *et al.* [60]. Comparing DFT results for different anions [53] or GW calculations for the same anion at different sophistication levels [13] shows instead that larger gaps have larger effective masses (see Fig. S3, Supplemental Material [39], which also includes Refs. [33, 53, 61]). To check for a similar trend, we also conducted a calculation for the orthorhombic unit cell and obtained a hole effective mass value of $m_{\mathrm{h}}^{*} = 0.226\ m_0$ averaged over the different crystallographic directions at a band gap of 2.09 eV, which is closer to the experi-

mental value of 2.37 eV [52] than other calculations (see Figs. S4, and S5 in the Supplemental Material [39]). This m_h^* value is even slightly larger than our ARPES result. Because Wannierization was only performed for the valence band, there is the possibility that the effective mass is slightly overestimated in the orthorhombic calculation. We believe that such overestimation is, on the other hand, rather limited. Note that, in our cubic calculation, as well as in that of Ref. [33], Wannierization was performed for valence and conduction bands and still the effective masses differ substantially (0.15 m_0 in the present case and 0.12 m_0 in Ref. [33]). We conclude that the measured effective mass can be explained by electron-electron correlations included in our theoretical description and does not indicate large-polaron formation.

As pointed out before [33], the LO phonon energy of $CsPbBr_3$ is very small ($\leq$ 25 meV) and satellites in ARPES should be difficult to observe. This raises the question whether lead halide perovskites are the right model systems for the observation of polaron formation and tin halide perovskites with phonon energies of more than 180 meV in $CsSnBr_3$ [62] are not suited better. DFT calculations [63] indicate a rise in the polaron stabilization energies upon exchange of Pb by Sn in $MAPbI_3$.

We showed that ARPES provides high-quality band structure data of halide perosvkites and helps assessing relevant physics for lead halide perovskites. Recently, we demonstrated by ARPES that a large valence band Rashba effect is absent in $MAPbBr_3$ and $CsPbBr_3$ [35]. We further note that small-polarons cannot be detected through the effective mass. While small polarons can cause deterioration of device performance by charge trapping [18, 63], it has recently been pointed out that in $CsPbBr_3$ small polarons can also reduce carrier recombination [64]. The experimental temperature-dependent charge mobility of lead halide perovskites was found not to be as supportive for the Fröhlich model of large polarons as was previously believed, and also compatible with small polaron formation [64]. Moreover, recent calculations suggest that polaronic effects on scattering and mobilities of charge carriers are more limited than previously claimed [65].

In conclusion, our experimental hole effective mass lies in between the results of our *GW* calculations, and despite recent success of Fröhlich polaron-based models for transport data, we do not find any significant mass enhancement, regardless of whether we compare to the cubic or the orthorhombic calculation. Our results are based on two insights: First, a precise determination of the point in momentum space is necessary for extracting the correct effective mass from the experiment. Second, the determination of the theoretical effective mass requires a calculation that does not strongly underestimate the band gap. The supporting data for the calculations in this Letter are openly available from the Materials Cloud repository [66].

ACKNOWLEDGEMENTS

We thank Professor Thomas Kirchartz for helpful discussions and continuous support and Professor Eva Unger for drawing our attention to $CsPbBr_3$. Use of the Helmholtz Innovation Lab HySPRINT for sample preparation is gratefully acknowledged as well as computing time granted through JARA-HPC on the supercomputer JURECA at Forschungszentrum Jülich. J. S.-B. gratefully acknowledges financial support from the Impuls- und Vernetzungsfonds der Helmholtz-Gemeinschaft under Grant No. HRSF-0067.

* Present address: Institute of Physics, University of Amsterdam, Science Park 904, 1098 XH Amsterdam, Netherlands.

[1] A. Al-Ashouri, E. Köhnen, B. Li, A. Magomedov, H. Hempel, P. Caprioglio, J. A. Márquez, A. B. Morales Vilches, E. Kasparavicius, J. A. Smith, N. Phung, D. Menzel, M. Grischek, L. Kegelmann, D. Skroblin, C. Gollwitzer, T. Malinauskas, M. Jošt, G. Matič, B. Rech, R. Schlatmann, M. Topič, L. Korte, A. Abate, B. Stannowski, D. Neher, M. Stolterfoht, T. Unold, V. Getautis, and S. Albrecht, Monolithic perovskite/silicon tandem solar cell with > 29% efficiency by enhanced hole extraction, Science **370**, 1300 (2020).

[2] T.-C. Sum and N. Mathews, *Halide Perovskites: Photovoltaics, Light Emitting Devices, and Beyond* (Wiley-VCH, Weinheim, 2019).

[3] K. X. Steirer, P. Schulz, G. Teeter, V. Stevanovic, M. Yang, K. Zhu, and J. J. Berry, Defect tolerance in methylammonium lead triiodide perovskite, ACS Energy Lett. **1**, 360 (2016).

[4] J. M. Ball and A. Petrozza, Defects in perovskite-halides and their effects in solar cells, Nat. Energy **1**, 16149 (2016).

[5] A. Biewald, N. Giesbrecht, T. Bein, P. Docampo, A. Hartschuh, and R. Ciesielski, Temperature-Dependent Ambipolar Charge Carrier Mobility in Large-Crystal Hybrid Halide Perovskite Thin Films, ACS Appl. Mater. Interfaces **11**, 20838 (2019).

[6] L. M. Herz, Charge-carrier mobilities in metal halide perovskites: fundamental mechanisms and limits, ACS Energy Lett. **2**, 1539 (2017).

[7] D. W. de Quilettes, K. Frohna, D. Emin, T. Kirchartz, V. Bulovic, D. S. Ginger, and S. D. Stranks, Charge-carrier recombination in halide perovskites: Focus review, Chem. Rev. **119**, 11007 (2019).

[8] D. Ghosh, E. Welch, A. J. Neukirch, A. Zakhidov, and S. Tretiak, Polarons in halide perovskites: A perspective, J. Phys. Chem. Lett. **11**, 3271 (2020).

[9] H. Jin, E. Debroye, M. Keshavarz, I. G. Scheblykin, M. B. J. Roeffaers, J. Hofkens, and J. A. Steele, It's a trap! On the nature of localised states and charge

trapping in lead halide perovskites, Mater. Horiz. **7**, 397 (2020).
[10] H. Zhang, X. Liu, J. Dong, H. Yu, C. Zhou, B. Zhang, Y. Xu, and W. Jie, Centimeter-sized inorganic lead halide perovskite $CsPbBr_3$ crystals grown by an improved solution method, Cryst. Growth Des. **17**, 6426 (2017).
[11] W. Götz, L. Romano, J. Walker, N. M. Johnson, and R. J. Molnar, Hall-effect analysis of GaN films grown by hydride vapor phase epitaxy, Appl. Phys. Lett. **72**, 1214 (1998).
[12] D. Shi, V. Adinolfi, R. Comin, M. Yuan, E. Alarousu, A. Buin, Y. Chen, S. Hoogland, A. Rothenberger, K. Katsiev, Y. Losovyj, X. Zhang, P. A. Dowben, O. F. Mohammed, E. H. Sargent, and O. M. Bakr, Low trap-state density and long carrier diffusion in organolead trihalide perovskite single crystals, Science **347**, 519 (2015).
[13] S. Poncé, M. Schlipf, and F. Giustino, Origin of low carrier mobilities in halide perovskites, ACS Energy Lett. **4**, 456 (2019).
[14] X.-Y. Zhu and V. Podzorov, Charge Carriers in Hybrid Organic-Inorganic Lead Halide Perovskites Might Be Protected as Large Polarons, J. Phys. Chem. Lett. **6**, 4758 (2015).
[15] P. P. Joshi, S. F. Maehrlein, and X. Zhu, Dynamic screening and slow cooling of hot carriers in lead halide perovskites, Adv. Mater. **31**, 1803054 (2019).
[16] F. Zheng and L.-w. Wang, Large polaron formation and its effect on electron transport in hybrid perovskites, Energy Environ. Sci. **12**, 1219 (2019).
[17] D. Emin, Barrier to recombination of oppositely charged large polarons, J. Appl. Phys. **123**, 055105 (2018).
[18] A. J. Neukirch, W. Nie, J.-C. Blancon, K. Appavoo, H. Tsai, M. Y. Sfeir, C. Katan, L. Pedesseau, J. Even, J. J. Crochet *et al.*, Polaron stabilization by cooperative lattice distortion and cation rotations in hybrid perovskite materials, Nano Lett. **16**, 3809 (2016).
[19] M. Bonn, K. Miyata, E. Hendry, and X.-Y. Zhu, Role of dielectric drag in polaron mobility in lead halide perovskites, ACS Energy Lett. **2**, 2555 (2017).
[20] H. Zhu, K. Miyata, Y. Fu, J. Wang, P. P. Joshi, D. Niesner, K. W. Williams, S. Jin, and X.-Y. Zhu, Screening in crystalline liquids protects energetic carriers in hybrid perovskites, Science **353**, 1409 (2016).
[21] K. Miyata, D. Meggiolaro, M. T. Trinh, P. P. Joshi, E. Mosconi, S. C. Jones, F. De Angelis, and X.-Y. Zhu, Large polarons in lead halide perovskites, Sci. Adv. **3**, e1701217 (2017).
[22] K. Miyata, T. L. Atallah, and X.-Y. Zhu, Lead halide perovskites: Crystal-liquid duality, phonon glass electron crystals, and large polaron formation, Sci. Adv. **3**, e1701469 (2017).
[23] J. M. Frost, L. D. Whalley, and A. Walsh, Slow cooling of hot polarons in halide perovskite solar cells, ACS Energy Lett. **2**, 2647 (2017).
[24] C. Q. Xia, J. Peng, S. Poncé, J. B. Patel, A. D. Wright, T. W. Crothers, M. Uller Rothmann, J. Borchert, R. L. Milot, H. Kraus, Q. Lin, F. Giustino, L. M. Herz, and M. B. Johnston, Limits to electrical mobility in lead-halide perovskite semiconductors, J. Phys. Chem. Lett. **12**, 3607 (2021).
[25] M. Schlipf, S. Poncé, and F. Giustino, Carrier lifetimes and polaronic mass enhancement in the hybrid halide perovskite $CH_3NH_3PbI_3$ from multiphonon fröhlich coupling, Phys. Rev. Lett. **121**, 086402 (2018).
[26] S. Hüfner, *Photoelectron spectroscopy: principles and applications* (Springer, Berlin, 2013).
[27] J. Jaćimović, C. Vaju, A. Magrez, H. Berger, L. Forró, R. Gaal, V. Cerovski, and R. Žikić, Pressure dependence of the large-polaron transport in anatase TiO_2 single crystals, EPL **99**, 57005 (2012).
[28] S. Moser, L. Moreschini, J. Jaćimović, O. S. Barišić, H. Berger, A. Magrez, Y. J. Chang, K. S. Kim, A. Bostwick, E. Rotenberg *et al.*, Tunable polaronic conduction in anatase TiO_2, Phys. Rev. Lett. **110**, 196403 (2013).
[29] C. Verdi, F. Caruso, and F. Giustino, Origin of the crossover from polarons to Fermi liquids in transition metal oxides, Nat. Commun. **8**, 15769 (2017).
[30] J. M. L. Van Mechelen, D. Van der Marel, C. Grimaldi, A. B. Kuzmenko, N. P. Armitage, N. Reyren, H. Hagemann, and I. I. Mazin, Electron-phonon interaction and charge carrier mass enhancement in $SrTiO_3$, Phys. Rev. Lett. **100**, 226403 (2008).
[31] C. Chen, J. Avila, E. Frantzeskakis, A. Levy, and M. C. Asensio, Observation of a two-dimensional liquid of Fröhlich polarons at the bare $SrTiO_3$ surface, Nat. Commun. **6**, 9585 (2015).
[32] Z. Wang, S. M. Walker, A. Tamai, Y. Wang, Z. Ristic, F. Y. Bruno, A. De La Torre, S. Riccò, N. C. Plumb, M. Shi *et al.*, Tailoring the nature and strength of electron–phonon interactions in the $SrTiO_3$ (001) 2D electron liquid, Nat. Mater. **15**, 835 (2016).
[33] M. Puppin, S. Polishchuk, N. Colonna, A. Crepaldi, D. N. Dirin, O. Nazarenko, R. De Gennaro, G. Gatti, S. Roth, T. Barillot *et al.*, Evidence of large polarons in photoemission band mapping of the perovskite semiconductor $CsPbBr_3$, Phys. Rev. Lett. **124**, 206402 (2020).
[34] Y. Rakita, N. Kedem, S. Gupta, A. Sadhanala, V. Kalchenko, M. L. Böhm, M. Kulbak, R. H. Friend, D. Cahen, and G. Hodes, Low-temperature solution-grown $CsPbBr_3$ single crystals and their characterization, Cryst. Growth Des. **16**, 5717 (2016).
[35] M. Sajedi, M. Krivenkov, D. Marchenko, A. Varykhalov, J. Sánchez-Barriga, E. D. L. Rienks, and O. Rader, Absence of a giant Rashba effect in the valence band of lead halide perovskites, Phys. Rev. B **102**, 081116(R) (2020).
[36] `www.flapw.de`.
[37] C. Friedrich, S. Blügel, and A. Schindlmayr, Efficient implementation of the GW approximation within the all-electron flapw method, Phys. Rev. B **81**, 125102 (2010).
[38] I. Aguilera, C. Friedrich, and S. Blügel, Spin-orbit coupling in quasiparticle studies of topological insulators, Phys. Rev. B **88**, 165136 (2013).
[39] See Supplemental Material for more information about our GW calculations, more ARPES data, a comparison of effective masses versus gaps in the literature, GW bands for the orthorhombic structure, and benchmarking of our GW gap.
[40] J. P. Perdew, K. Burke, and M. Ernzerhof, Generalized gradient approximation made simple, Phys. Rev. Lett. **77**, 3865 (1996).
[41] D. Koelling and B. Harmon, A technique for relativistic spin-polarised calculations, J. Phys. C: Solid State Phys. **10**, 3107 (1977).
[42] C. Li, A. J. Freeman, H. J. F. Jansen, and C. L. Fu, Magnetic anisotropy in low-dimensional ferromagnetic systems: Fe monolayers on Ag(001), Au(001), and Pd(001) substrates, Phys. Rev. B **42**, 5433 (1990).
[43] A. A. Mostofi, J. R. Yates, Y.-S. Lee, I. Souza, D. Van-

derbilt, and N. Marzari, wannier90: A tool for obtaining maximally-localised Wannier functions, Comput. Phys. Commun. **178**, 685 (2008).

[44] K. Lejaeghere, G. Bihlmayer, T. Björkman, P. Blaha, S. Blügel, V. Blum, D. Caliste, I. E. Castelli, S. J. Clark, A. Dal Corso *et al.*, Reproducibility in density functional theory calculations of solids, Science **351**, aad3000 (2016).

[45] K. Persson, Materials data on $CsPbBr_3$ (sg:62) by materials project 10.17188/1273967 (2014).

[46] K. Persson, Materials data on $CsPbBr_3$ (sg:221) by materials project 10.17188/1272881 (2014).

[47] M. Rodová, J. Brožek, K. Knížek, and K. Nitsch, Phase transitions in ternary caesium lead bromide, J. Therm. Anal. Calorim. **71**, 667 (2003).

[48] S. Hirotsu, J. Harada, M. Iizumi, and K. Gesi, Structural phase transitions in $CsPbBr_3$, J. Phys. Soc. Jpn. **37**, 1393 (1974).

[49] M. Zhang, Z. Zheng, Q. Fu, Z. Chen, J. He, S. Zhang, L. Yan, Y. Hu, and W. Luo, Growth and characterization of all-inorganic lead halide perovskite semiconductor $CsPbBr_3$ single crystals, Cryst. Eng. Comm. **19**, 6797 (2017).

[50] J. M. Frost, K. T. Butler, F. Brivio, C. H. Hendon, M. Van Schilfgaarde, and A. Walsh, Atomistic origins of high-performance in hybrid halide perovskite solar cells, Nano Lett. **14**, 2584 (2014).

[51] M. G. Goesten and R. Hoffmann, Mirrors of bonding in metal halide perovskites, J. Am. Chem. Soc. **140**, 12996 (2018).

[52] G. Mannino, I. Deretzis, E. Smecca, A. La Magna, A. Alberti, D. Ceratti, and D. Cahen, Temperature-dependent optical band gap in $CsPbBr_3$, $MAPbBr_3$, and $FAPbBr_3$ single crystals, J. Phys. Chem. Lett. **11**, 2490 (2020).

[53] Y. Kang and S. Han, Intrinsic carrier mobility of cesium lead halide perovskites, Phys. Rev. Applied **10**, 044013 (2018).

[54] J. Wiktor, U. Rothlisberger, and A. Pasquarello, Predictive determination of band gaps of inorganic halide perovskites, J. Phys. Chem. Lett. **8**, 5507 (2017).

[55] R. Rajeswarapalanichamy, A. Amudhavalli, R. Padmavathy, and K. Iyakutti, Band gap engineering in halide cubic perovskites $CsPbBr_{3-y}I_y$ (y= 0, 1, 2, 3)–A *DFT* study, Mater. Sci. Eng., B **258**, 114560 (2020).

[56] Y. Ye, X. Run, X. Hai-Tao, H. Feng, X. Fei, and W. Lin-Jun, Nature of the band gap of halide perovskites ABX_3 (A= CH_3NH_3, Cs; B= Sn, Pb; X= Cl, Br, I): First-principles calculations, Chin. Phys. B **24**, 116302 (2015).

[57] H. M. Ghaithan, Z. A. Alahmed, S. M. Qaid, M. Hezam, and A. S. Aldwayyan, Density functional study of cubic, tetragonal, and orthorhombic $CsPbBr_3$ perovskite, ACS Omega **5**, 7468 (2020).

[58] J. Qian, B. Xu, and W. Tian, A comprehensive theoretical study of halide perovskites ABX_3, Org. Electron. **37**, 61 (2016).

[59] J. Sun, J. Yang, and C. A. Ullrich, Low-cost alternatives to the Bethe-Salpeter equation: Towards simple hybrid functionals for excitonic effects in solids, Phys. Rev. Res. **2**, 013091 (2020).

[60] M. A. Becker, R. Vaxenburg, G. Nedelcu, P. C. Sercel, A. Shabaev, M. J. Mehl, J. G. Michopoulos, S. G. Lambrakos, N. Bernstein, J. L. Lyons *et al.*, Bright triplet excitons in caesium lead halide perovskites, Nature **553**, 189 (2018).

[61] M. R. Filip, C. Verdi, and F. Giustino, *GW* band structures and carrier effective masses of $CH_3NH_3PbI_3$ and hypothetical perovskites of the type $APbI_3$: A= NH_4, PH_4, AsH_4, and SbH_4, J. Phys. Chem. C **119**, 25209 (2015).

[62] L.-y. Huang and W. R. L. Lambrecht, Electronic band structure, phonons, and exciton binding energies of halide perovskites $CsSnCl_3$, $CsSnBr_3$, and $CsSnI_3$, Phys. Rev. B **88**, 165203 (2013).

[63] D. Meggiolaro, F. Ambrosio, E. Mosconi, A. Mahata, and F. De Angelis, Polarons in metal halide perovskites, Adv. Energy Mater. **10**, 1902748 (2020).

[64] N. Österbacka, P. Erhart, S. Falletta, A. Pasquarello, and J. Wiktor, Small electron polarons in $CsPbBr_3$: Competition between electron localization and delocalization, Chem. Mater. **32**, 8393 (2020).

[65] L. A. D. Irvine, A. B. Walker, and M. J. Wolf, Quantifying polaronic effects on the scattering and mobility of charge carriers in lead halide perovskites, Phys. Rev. B **103**, L220305 (2021).

[66] M. Sajedi, M. Krivenkov, D. Marchenko, J. Sánchez-Barriga, A. K. Chandran, A. Varykhalov, E. D. L. Rienks, I. Aguilera, S. Blügel, and O. Rader, Is There a Polaron Signature in Angle-Resolved Photoemission of $CsPbBr_3$?, Materials Cloud Archive 2022.51 10.24435/MATERIALSCLOUD:93-J5 (2022).